

# Non-hotspot volcano chains produced by migration of shear-driven upwelling toward the East Pacific Rise

**Maxim D. Ballmer<sup>1</sup>, Clinton P. Conrad<sup>1</sup>, Eugene I. Smith<sup>2</sup>, and Nicholas Harmon<sup>3</sup>**

<sup>1</sup>*Department of Geology and Geophysics, School of Ocean and Earth Sciences and Technology, University of Hawaii at Manoa, Honolulu, Hawaii 96822, USA*

<sup>2</sup>*Department of Geoscience, University of Nevada Las Vegas, Las Vegas, Nevada 89154, USA*

<sup>3</sup>*National Oceanography Centre Southampton, Ocean and Earth Science, University of Southampton, Southampton SH14 3ZH, UK*

## Data Repository

### Methods and Model Setup

We model fluid flow in a rectangular box 300 km deep, 150 km wide and 2736 km long. The model domain is discretized in 112x64x768 to 112x64x960 finite elements, in which the equations of conservation of mass, momentum and energy are solved using the code CITCOM (Moresi and Gurnis, 1996; Zhong et al., 2000). Grid refinement increases the resolution to a maximum of 2.19x2.34x2.27 km<sup>3</sup> close to the surface (and at ~900 km away from the back side of the box). We generally apply the Boussinesq approximations, and additionally account for the effects adiabatic heating and latent heat of melting. Passive particles trace the advection of non-diffusive properties (i.e., composition). Details of the numerical method — including the parameterizations for melting (Katz et al., 2003; Pertermann and Hirschmann, 2003), dehydration, compositional buoyancy, and compositional rheology — are reported in Ballmer et al. (2009) and Ballmer (2009). Key parameters are given in Table DR1. An important modification to our previous work is that in order to focus on the effects of SDU we switch off melt buoyancy. We find in benchmark tests that switching melt buoyancy on only moderately increases volumes of volcanism, and leaves the overall behavior unchanged (Fig. DR5).

Velocity boundary conditions impose a first-order flow pattern within the computational box. The boundaries are closed at the sides, as well as at the top and bottom, but they remain open to inflow and outflow at both the front and the back (cf. Figs. 2a,

DR3a). At the top boundary, we impose a velocity boundary condition of  $v_{Pacific} = -7$  cm/a and  $v_{Nazca} = 10$  cm/a at distances greater and smaller than 900 km from the back side (i.e. eastern) boundary, respectively. These boundary conditions simulate the motion of the Pacific and Nazca Plates, respectively. Further, they impose a spreading center parallel to, and 900 km away from, the back side of the box. At the back side, a negative pressure is applied that drives eastward Poiseuille flow within the asthenospheric channel. At the back side of the box, the maximum of this flow component is  $v_{Poiseuille} = 5.333$  cm/a. Due to an additional negative pressure that is created at the MOR by the spreading plates, however, eastward Poiseuille flow organizes with significantly greater amplitudes in the asthenospheric channel towards the front side of the box (i.e., beneath the simulated Pacific Plate; cf. Fig. 2a, DR3a). Finally, at the bottom boundary, we apply a velocity condition of  $v_{Bottom} = 0.5v_{Poiseuille}$  in order to account for the expected extension of Poiseuille flow into the transition zone, a depth range that is not modeled explicitly. The resulting combined vertical profiles of Poiseuille and Couette flow at the front and back boundaries are shown in Figs. 2a and DR3a. Migration of the spreading center is neglected, although it has been shown to somewhat influence mantle dynamics (Conder et al., 2002; Toomey et al., 2002). However, by comparing case A with a simulation that accounts for westward ridge migration by setting  $v_{Pacific} = v_{Nazca} = 7.2$  cm/a,  $v_{Bottom} = 5.333$  cm/a and  $v_{Poiseuille} = 6.667$  cm/a, we find that this assumption only marginally influences our results. Our velocity boundary conditions (Figs. 2a, DR3a) are indeed in accord with those predicted in Conrad and Behn (2010) for the asthenosphere beneath the southeast Pacific (Fig. DR2).

Temperature boundary and initial conditions account for half-space cooling in both directions away from the spreading center, and impose constant temperatures at the top ( $T_{top} = 0$  °C) and bottom ( $T_{bottom}$ ):  $T_{bottom} = T_{ref} + d\gamma$  with  $d$  the depth of the box,  $T_{ref} = 1350$  °C the reference temperature, and  $\gamma$  the adiabatic gradient (cf. Table DR1). The side boundaries are reflective, a setup that implies a characteristic wavelength of 300 km for the channeling instability that creates the low-viscosity fingers. This assumption is consistent with the spacing of cross-grain gravity lineations in the study area.

While the imposed boundary conditions set up the flow pattern that is required to satisfy first-order geophysical constraints in the study area (Conder et al., 2002; Toomey et al., 2002), the crucial ingredient for our models is the initial condition of a low-viscosity finger. We impose a rectangular anomaly close to the front corner of the box (Figs. 2a, DR3a). The full width of this anomaly is 150 km, but by assuming symmetry only half of this width is actually modeled. Its length and vertical extent are 600 km and 90 km, respectively; its average depth is 135 km. Accordingly, the initial depths of its top and bottom are 90 and 180 km, respectively. The initial viscosity in the finger is a factor of  $\eta_{mantle}/\eta_{finger} = 47$  smaller than that of the ambient mantle.

In order to sustain this viscosity contrast, we increase the finger water content relative to the ambient-mantle bulk water content of 27.19 ppm (Fig. DR3a, Table DR2). In some simulations, we also increase the finger temperature. In these cases, we adjust the finger water content to keep  $\eta_{mantle}/\eta_{finger} = 47$ , or to modulate  $\eta_{mantle}/\eta_{finger}$  (Fig. 2a, Table DR2). The imposed initial crossover in water content (and in temperature) is gradual: it is released linearly over a distance of 12 km at each side of the finger, a setup that effectively increases its size by 10-20 km in each dimension. Furthermore, the water content and temperature in the shallowest part of the finger are reduced in order to keep the entire finger at (or below) the applied solidus (Katz et al., 2003). This reduction is done in order to avoid melting in the first time-step, and effectively reduces the vertical extent of the finger and increases its average depth, particularly for models with high finger temperatures. Elevated effective water contents in the asthenosphere beneath the SE Pacific are consistent with geophysical constraints (Karato, 2008).

In cases C1-C5, we add a small share of fertile material to the mantle. We use pyroxenite as representative of the fertile component. The melting law for pyroxenite is taken from (Pertermann and Hirschmann, 2003). Pyroxenite makes up 2-7% of the initial finger (2% in case C1, 3% in case C2, 4% in case C3, 5% in case C4, and 7% in case C5), and 2% of the ambient mantle. In cases C1-C4, 95% of the ambient mantle and the finger are peridotite (with the remainder being a refractory component that does not contribute to melting). In case C5, 93% of the ambient mantle is peridotite. The effects of pyroxenite and the refractory component on bulk density and bulk viscosity are neglected. Additional details of our multi-lithological approach and the melting parameterizations are described in Ballmer et al. (Ballmer et al., 2010; Ballmer et al., 2009) and Ballmer (2009).

| Parameter                                       | symbol                        | Value   |
|---|-------------------------------|---|
| activation energy <sup>abc</sup>                | $E^*$                         | 200 kJ/mol  |
| activation volume                               | $V^*$                         | $5 \cdot 10^{-6} \text{ m}^3/\text{mol}$            |
| effective mantle viscosity                      | $\eta_{mantle}$               | $\sim 2.25 \cdot 10^{19} \text{ Pa} \cdot \text{s}$ |
| latent heat of melt                             | $L$                           | 560 kJ/kg   |
| reference temperature                           | $T_{ref}$                     | 1350 °C   |
| magma extraction threshold                      | $\varphi_C$                   | 0.5%  |
| dehydration stiffening coefficient <sup>d</sup> | $\zeta$                       | 100   |
| melt lubrication exponent <sup>e</sup>          | $\zeta$                       | -40   |
| mantle density                                  | $\rho_{ref}$                  | 3300 kg/m <sup>3</sup>                              |
| magma density                                   | $\rho_{melt}$                 | 2800 kg/m <sup>3</sup> ; 3300 kg/m <sup>3</sup>     |
| depletion buoyancy <sup>f</sup>                 | $\Delta\rho_{depl}$           | -72.6 kg/m <sup>3</sup>                             |
| depth of the box                                | $d$                           | 300 km  |
| adiabatic gradient                              | $\gamma$                      | 0.38882 K/km  |
| viscosity contrast                              | $\eta_{mantle}/\eta_{finger}$ | 1; 47   |
| bulk water content in the ambient mantle        | $c_0$                         | 27.19 ppm   |

**Table DR1:** notations. For additional parameters, cf. Table 2.1 in Ballmer (2009).  
<sup>a</sup>Christensen (1984), <sup>b</sup>Karato and Wu (1993), <sup>c</sup>Hirth (2002), <sup>d</sup>Hirth and Kohlstedt (1996),  
<sup>e</sup>Kohlstedt and Zimmerman (1996), <sup>f</sup>Schutt and Lesher (2006).

| Case                    | finger excess temperature (°C) | finger water content (ppm) | content of fertile component in the finger | $\eta_{mantle}/\eta_{finger}$ | $\rho_{melt}$          |
|-------------------------|--------------------------------|----------------------------|--|-------------------------------|------------------------|
| <b>A</b>                | 0                              | 800                        | 0%   | 47                            | 3300 kg/m <sup>3</sup> |
| <b>B</b>                | 60                             | 473.7701                   | 0%   | 47                            | 3300 kg/m <sup>3</sup> |
| <b>B'</b>               | 60                             | 244.3893                   | 0%   | 24                            | 3300 kg/m <sup>3</sup> |
| <b>B''</b>              | 60                             | 124.7195                   | 0%   | 12                            | 3300 kg/m <sup>3</sup> |
| <b>B'''</b>             | 60                             | 64.884                     | 0%   | 6                             | 3300 kg/m <sup>3</sup> |
| <b>C1</b>               | 60                             | 473.7701                   | 2%   | 47                            | 3300 kg/m <sup>3</sup> |
| <b>C2</b>               | 60                             | 473.7701                   | 3%   | 47                            | 3300 kg/m <sup>3</sup> |
| <b>C3</b>               | 60                             | 473.7701                   | 4%   | 47                            | 3300 kg/m <sup>3</sup> |
| <b>C4</b>               | 60                             | 473.7701                   | 5%   | 47                            | 3300 kg/m <sup>3</sup> |
| <b>C5</b>               | 60                             | 473.7701                   | 7%   | 47                            | 3300 kg/m <sup>3</sup> |
| <b>A</b>                | 0                              | 800                        | 0%   | 47                            | 2800 kg/m <sup>3</sup> |
| <b>B</b>                | 60                             | 473.7701                   | 0%   | 47                            | 2800 kg/m <sup>3</sup> |
| <b>A<sub>test</sub></b> | 0                              | 800                        | 0%   | 1                             | 3300 kg/m <sup>3</sup> |

**Table DR2:** controlling parameters for cases A and B, as well as for cases A<sub>test</sub>,  $\alpha$ ,  $\beta$ , and C1-C5.

| hypothetic end-member       | $\theta$ | $^{206}\text{Pb}/^{204}\text{Pb}$ | $^{207}\text{Pb}/^{204}\text{Pb}$ | $^{208}\text{Pb}/^{204}\text{Pb}$ | $^{87}\text{Sr}/^{86}\text{Sr}$ | $^{143}\text{Nd}/^{144}\text{Nd}$ |
|-----------------------------|----------|-----------------------------------|-----------------------------------|-----------------------------------|---------------------------------|-----------------------------------|
| SEPR (Mahoney et al., 1994) | 0        | 18.15                             | 15.45                             | 37.57                             | 0.70243                         | 0.513196                          |
| FOZO (Stracke et al., 2005) | 1        | 19.97                             | 15.6345                           | 39.56                             | 0.7038                          | 0.512873                          |

**Table DR3:** geochemical end-members used for the calculation of  $\theta$ .

## Supplemental Figures

**Figure DR1.** Schematic illustration of characteristic shear-driven flow as modeled here. Black arrows show a typical horizontal flow field in three profiles. The horizontal velocities result from a combination of Poiseuille (pressure-driven) and Couette (shear-driven) flows. The differences between the profiles are caused by the presence of the low-viscosity finger (purple box), and are accommodated by vertical flow (white arrows) near the edges of the low-viscosity finger.

**Figure DR2.** Predicted mantle density, viscosity and flow in the SE Pacific, from the global mantle flow model of Conrad and Behn (2010). **(a)** horizontal (arrows) and vertical (colors) mantle flow in a horizontal cross-section at 300 km depth. **(b)** mantle density (colors) and flow (arrows) for vertical cross-section a-d that crosses the SEPR close to the Pukapuka ridge (see inset in a). **(c)** mantle viscosity (colors) and flow (arrows) in the central part (b-c) of that same cross-section. Cross-section boundaries are denoted as a green line and labels in panel **(a)**.

**Figure DR3.** Three-dimensional time series of temperature and melting for case A (same as **Fig. 2**, but for case A). The width of the SDU melting zone systematically increases from panel **(e)** through **(g)**. Melting does not start before  $\sim 1.5$  Myr and only slowly intensifies through time. Also, compare **Movie DR2** in the Data Repository.

**Figure DR4.** Viscosity and melting for cases A **(a, b)** and B **(c)** for the initial condition **(a)**, and for the snapshot at which the low-viscosity finger reaches the MOR **(b, c)**. The dashed lines encircle zones of abundant melt. The thick solid line encircles the zone of significant melt extraction (i.e. where both magma production rate  $dF/dt > 0.17\%/Myr$ , and melt fractions are close to the critical porosity  $\varphi_c = 0.5\%$ ). Shading of increasing darkness denotes magma production of increasing vigor in the zone of active melt extraction. The

minimum viscosity in the finger remains almost constant through time for both cases (initial finger viscosities for case B (not shown) are similar to those for case A (**a**)). In case B (**c**), a partially molten layer in the finger extends  $\sim 1000$  km off-axis.

**Figure DR5.** Time-evolution of volcanism in various cases. Solid lines display volcanic fluxes related to magmatism in the low-viscosity finger for test cases  $\alpha$ ,  $A_{\text{test}}$ ,  $\beta$ ,  $B'$ ,  $B''$ , and  $B'''$  (Table DR2). For reference, dashed lines show volcanic fluxes for cases A and B. Areas in the diagram with non-representatively large volcanic fluxes are flagged by the brown and yellow fields. Direct comparison of cases A and  $\alpha$ , as well as B and  $\beta$  elucidates that melt retention buoyancy does not significantly boost volcanism. The results of the model series with cases  $B'$ ,  $B''$ , and  $B'''$  show that viscosity contrasts of  $\eta_{\text{mantle}}/\eta_{\text{finger}} \gtrsim 20$  are required for significant intraplate volcanism from SDU. Case  $A_{\text{test}}$ , in which SDU is artificially switched off ( $\eta_{\text{mantle}}/\eta_{\text{finger}} = 1$ ), displays no off-axis volcanism.

[Movie DR1](#)

[Movie DR2](#)

## References

- Ballmer, M. D., 2009, Small-scale sublithospheric convection - an alternative mechanism for oceanic intraplate volcanism [Ph.D.: Diss. ETH No. 18425, ETH Zürich.
- Ballmer, M. D., Ito, G., van Hunen, J., and Tackley, P. J., 2010, Small-scale sublithospheric convection reconciles geochemistry and geochronology of 'Superplume' volcanism in the western and south Pacific: *Earth Plan. Sci. Lett.*, v. 290, no. 1-2, p. 224-232.
- Ballmer, M. D., van Hunen, J., Ito, G., Bianco, T. A., and Tackley, P. J., 2009, Intraplate volcanism with complex age-distance patterns – a case for small-scale sublithospheric convection: *Geochem. Geophys. Geosyst.*, v. 10, p. Q06015.
- Christensen, U., 1984, Convection with pressure-dependent and temperature-dependent non-Newtonian rheology: *Geophys. J. R. Astron. Soc.*, v. 77, no. 2, p. 343-384.
- Conder, J. A., Forsyth, D. W., and Parmentier, E. M., 2002, Asthenospheric flow and asymmetry of the East Pacific Rise, MELT area: *J. Geophys. Res.*, v. 107, no. B12, p. 15.
- Conrad, C. P., and Behn, M. D., 2010, Constraints on lithosphere net rotation and asthenospheric viscosity from global mantle flow models and seismic anisotropy: *Geochem. Geophys. Geosyst.*, v. 11.
- Hirth, G., 2002, Laboratory constraints on the rheology of the upper mantle: *Plastic Deformation of Minerals and Rocks*, v. 51, p. 97-120.

- Hirth, G., and Kohlstedt, D. L., 1996, Water in the Oceanic Upper-Mantle - Implications For Rheology, Melt Extraction and the Evolution of the Lithosphere: *Earth Planet. Sci. Lett.*, v. 144, no. 1-2, p. 93-108.
- Karato, S.-I., 2008, Insights into the nature of plume–asthenosphere interaction from central Pacific geophysical anomalies: *Earth Plan. Sci. Lett.*, v. 274, no. 1–2, p. 234-240.
- Karato, S., and Wu, P., 1993, Rheology of the upper mantle - a synthesis: *Science*, v. 260, no. 5109, p. 771-778.
- Katz, R. F., Spiegelman, M., and Langmuir, C. H., 2003, A new parameterization of hydrous mantle melting: *Geochem. Geophys. Geosyst.*, v. 4, no. 9, p. 1073.
- Kohlstedt, D. L., and Zimmerman, M. E., 1996, Rheology of partially molten mantle rocks: *Ann. Rev. Earth Planet. Sci.*, v. 24, p. 41-62.
- Mahoney, J. J., Sinton, J. M., Kurz, M. D., Macdougall, J. D., Spencer, K. J., and Lugmair, G. W., 1994, Isotope and Trace-element Characteristics of a super-fast Spreading Ridge - East Pacific Rise, 13-23-degrees-S: *Earth Plan. Sci. Lett.*, v. 121, no. 1-2, p. 173-193.
- Moresi, L., and Gurnis, M., 1996, Constraints on the lateral strength of slabs from 3-dimensional dynamic flow models: *Earth Planet. Sci. Lett.*, v. 138, no. 1-4, p. 15-28.
- Pertermann, M., and Hirschmann, M. M., 2003, Partial melting experiments on a MORB-like pyroxenite between 2 and 3 GPa: Constraints on the presence of pyroxenite in basalt source regions from solidus location and melting rate: *J. Geophys. Res.*, v. 108, no. B2, p. 2125.
- Schutt, D. L., and Leshner, C. E., 2006, Effects of melt depletion on the density and seismic velocity of garnet and spinel lherzolite: *J. Geophys. Res.*, v. 111, p. B05401, doi:05410.01029/02003JB002950.
- Stracke, A., Hofmann, A. W., and Hart, S., 2005, FOZO, HIMU, and the rest of the mantle zoo: *Geochem. Geophys. Geosyst.*, v. 6, no. Q05007, p. doi:10.1029/2004GC000824.
- Toomey, D. R., Wilcock, W. S. D., Conder, J. A., Forsyth, D. W., Blundy, J. D., Parmentier, E. M., and Hammond, W. C., 2002, Asymmetric mantle dynamics in the MELT region of the East Pacific Rise: *Earth Plan. Sci. Lett.*, v. 200, no. 3-4, p. 287-295.
- Zhong, S., Zuber, M. T., Moresi, L., and Gurnis, M., 2000, Role of temperature-dependent viscosity and surface plates in spherical shell models of mantle convection: *J. Geophys. Res.*, v. 105, no. B5, p. 11063-11082.

Fig. DR1

**LITHOSPHERE**

**FINGER**

**ASTHENOSPHERE**

**MESOSPHERE**

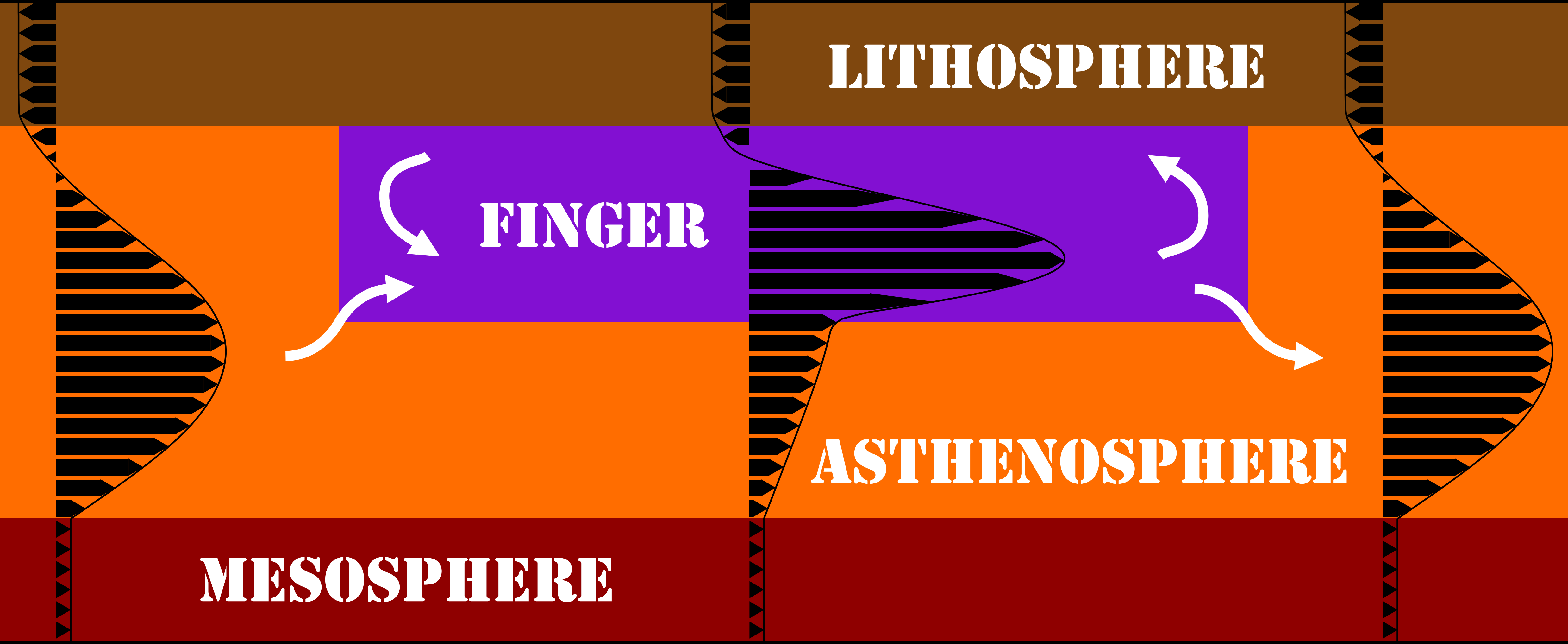
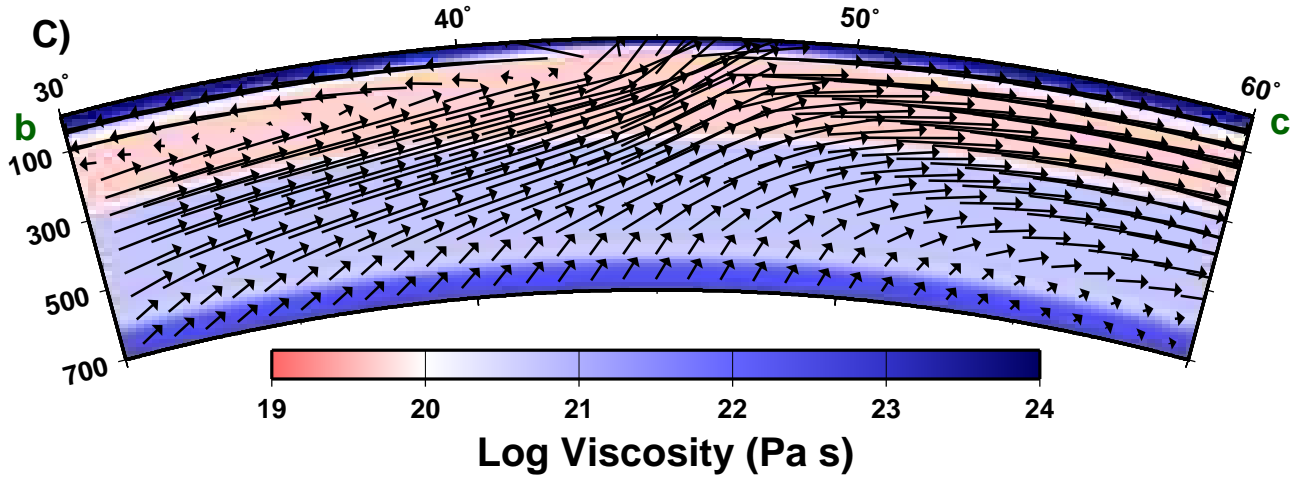
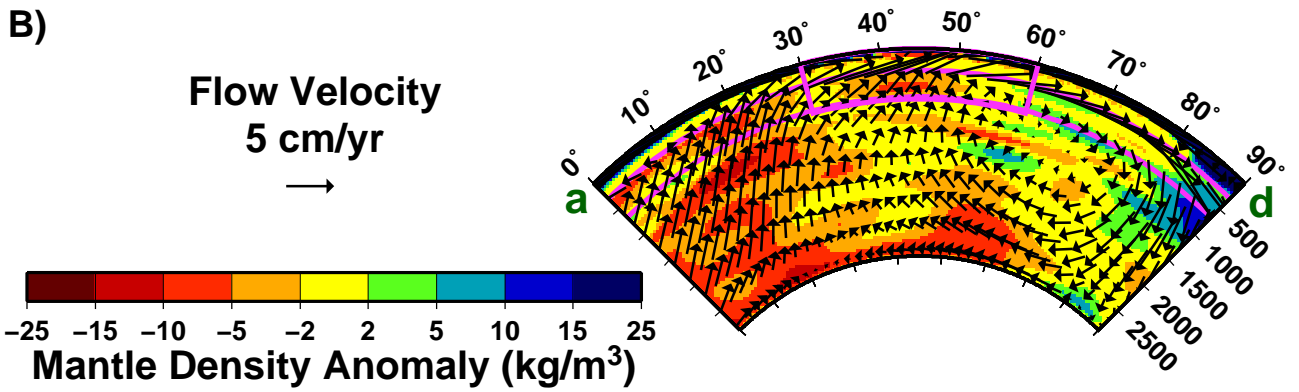
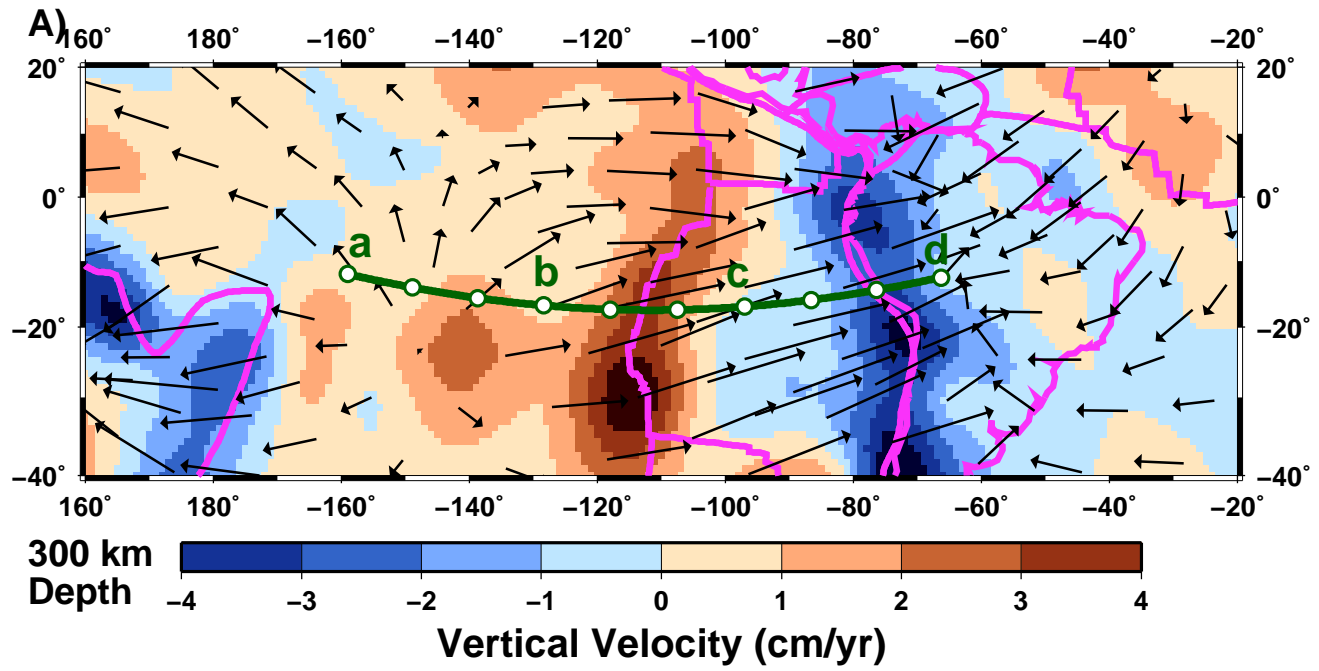


Figure DR2



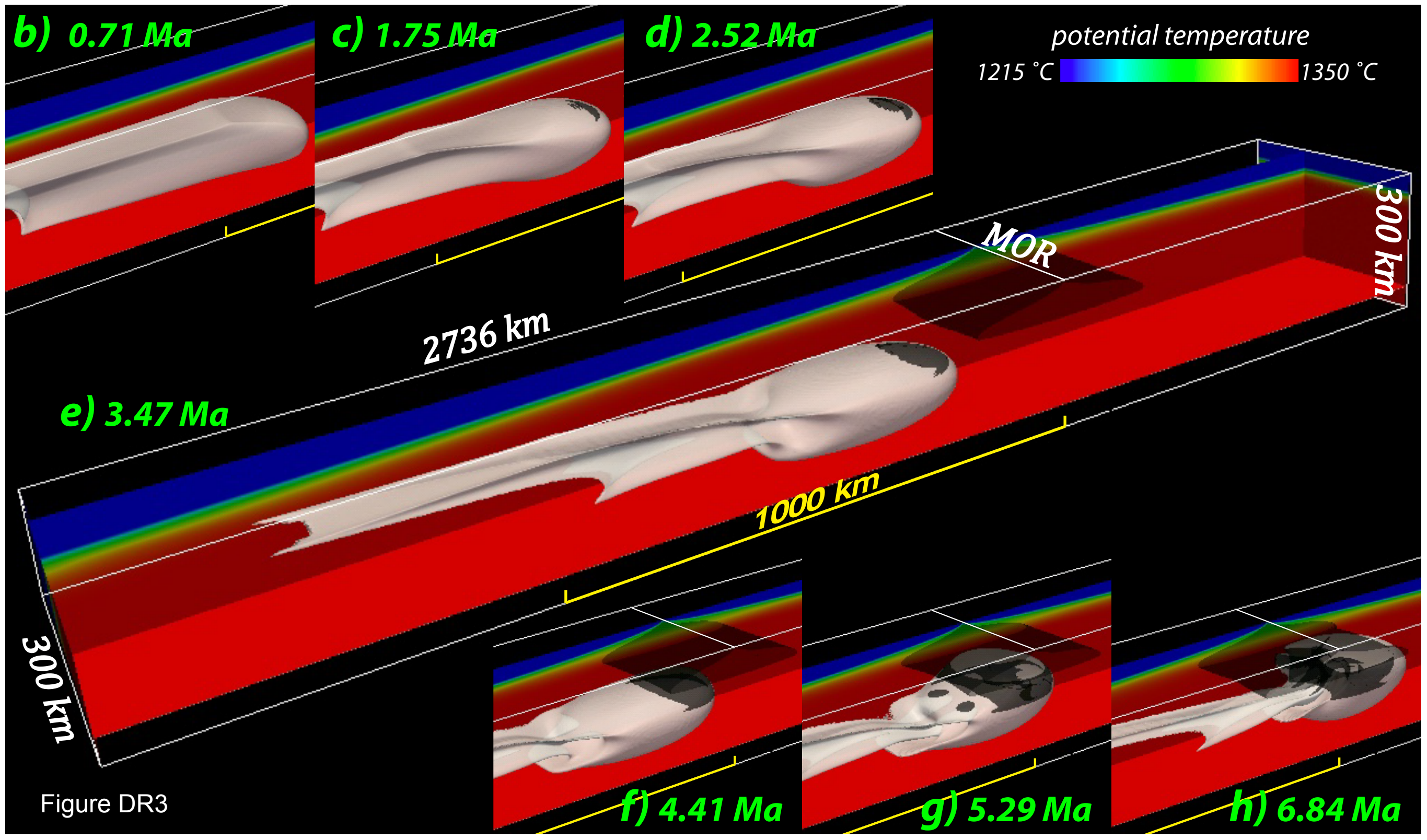
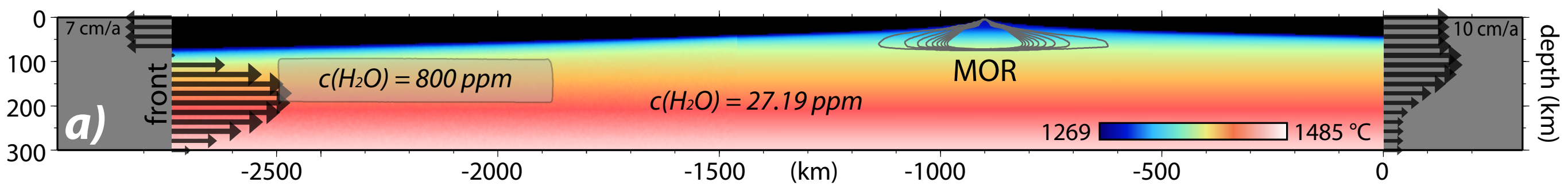
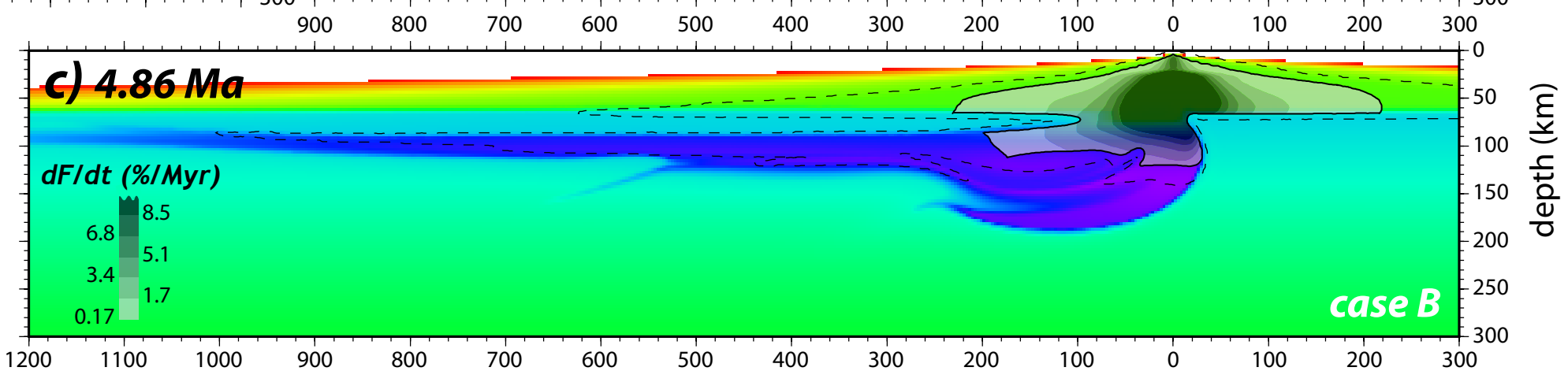
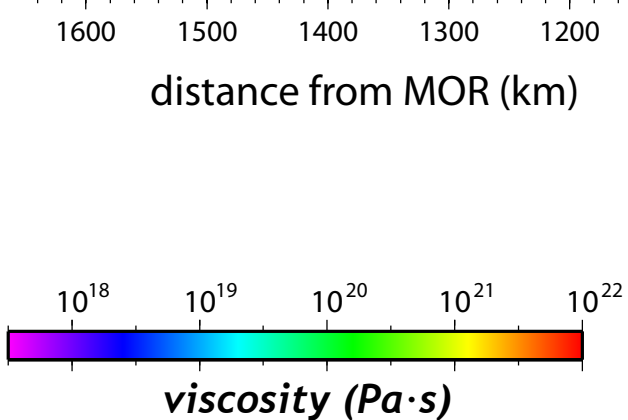
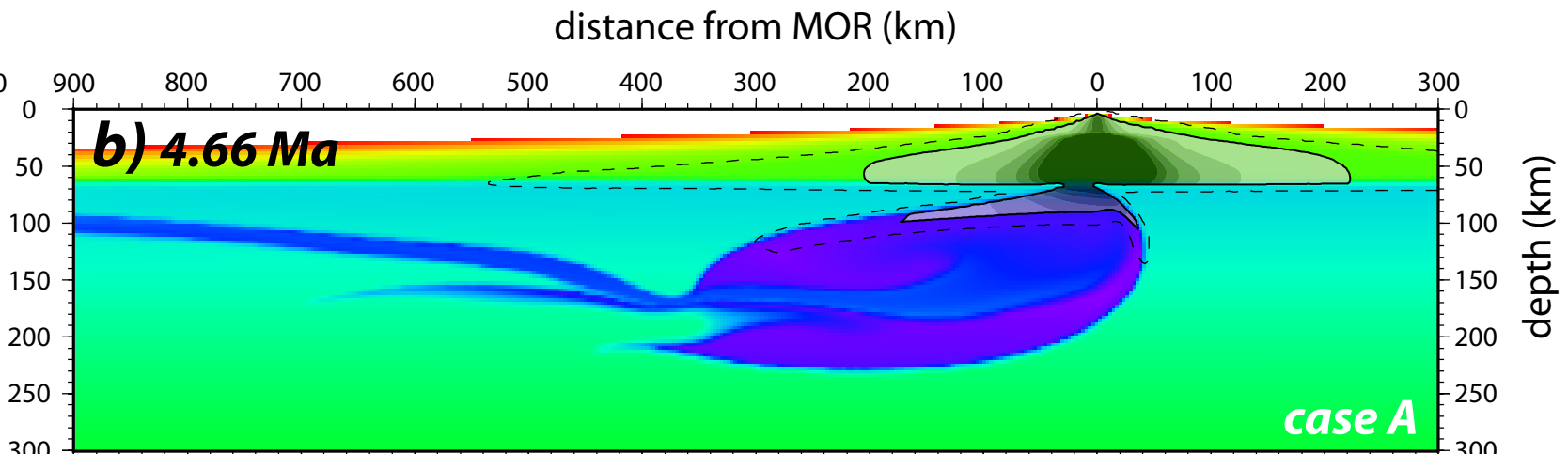
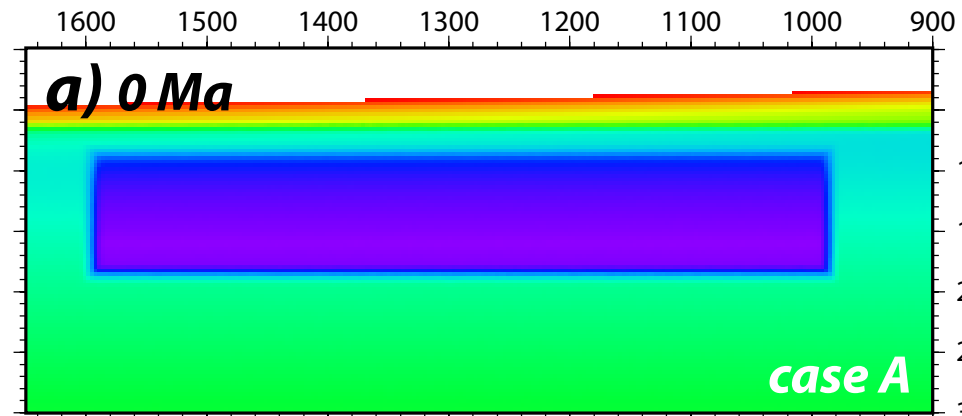


Figure DR3

Figure DR4 distance from MOR (km)



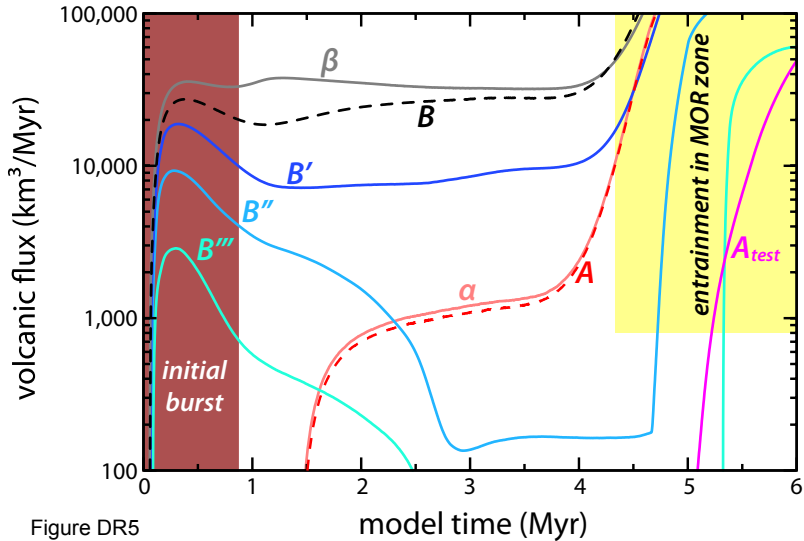


Figure DR5